

Electronic depth profiles with atomic layer resolution from resonant soft x-ray reflectivity

M. Zwiebler¹, J. E. Hamann-Borrero¹, M. Vafae², P. Komissinskiy², S. Macke^{3,4}, R. Sutarto⁵, F. He⁵, B. Büchner¹, G. A. Sawatzky⁶, L. Alff² and J. Geck¹

¹Leibniz Institute for Solid State and Materials Research, IFW-Dresden, Helmholtzstr. 20, 01069 Dresden, Germany

²Institute of Materials Science, Technische Universität Darmstadt, 64287 Darmstadt, Germany

³Max Planck-UBC Centre for Quantum Materials, Vancouver, V6T1Z1, Canada

⁴Max Planck Institute for Solid State Research, Heisenbergstr. 1, 70569 Stuttgart, Germany

⁵Canadian Light Source, University of Saskatchewan, Saskatoon, Saskatchewan, S7N0X4, Canada

⁶Department of Physics and Astronomy, University of British Columbia, Vancouver, V6T1Z1, Canada

Abstract. The analysis of x-ray reflectivity data from artificial heterostructures usually relies on the homogeneity of optical properties of the constituent materials. However, when the x-ray energy is tuned to an absorption edge, this homogeneity no longer exists. Within the same material, spatial regions containing elements at resonance will have optical properties very different from regions without resonating sites. In this situation, models assuming homogenous optical properties throughout the material can fail to describe the reflectivity adequately. As we show here, resonant soft x-ray reflectivity is sensitive to these variations, even though the wavelength is typically large as compared to the atomic distances over which the optical properties vary. We have therefore developed a scheme for analyzing resonant soft x-ray reflectivity data, which takes the atomic structure of a material into account by slicing it into atomic planes with characteristic optical properties. Using LaSrMnO_4 as an example, we discuss both the theoretical and experimental implications of this approach. Our analysis not only allows to determine important structural information such as interface terminations and stacking of atomic layers, but also enables to extract depth-resolved spectroscopic information with atomic resolution, thus enhancing the capability of the technique to study emergent phenomena at surfaces and interfaces.

1. Introduction

Specular x-ray reflectivity is one of the work horses for characterizing thin films and multilayers. In simple words, the reflectivity is given by interference of x-rays that are reflected at the different interfaces realized in such an artificial heterostructure. Referring to the reflection of optical light, an interface can be defined as a region in

space where there is a change of the refractive index n . Similarly, also in the x-ray range even a small change in n will introduce an interface, thus a traveling x-ray wave will be reflected. This high interface sensitivity is what allows to accurately determine structural properties of heterostructures such as layer thicknesses and interface roughnesses by means of x-ray reflectivity.

Recently, with the advent of synchrotron radiation, the availability of photon sources with very high brilliance and tunable energy has opened the frontiers for x-ray reflectivity techniques to study additional properties apart from structure. Electronic properties, for instance, can be studied by tuning the x-ray photon energies to an absorption edge. At these so-called resonant energies, the refractive index depends very strongly on the valence shell configuration of the resonant scattering centers and, hence, the sensitivity to spatial variations of the electronic properties is dramatically enhanced at resonances. This renders resonant x-ray reflectivity (RXR) an ideal tool to study electronic properties and phenomena at surfaces and buried interfaces in an element specific and non-destructive way.

The development of RXR was in particular triggered by the recent progress made in the atomic scale synthesis of transition metal oxide (TMO) heterostructures. TMOs provide perhaps one of the richest and fruitful fields in condensed matter research in terms of electronic properties and emerging novel physics [1–4]. Examples of these exotic phenomena are, among others, the formation of a two-dimensional electron gas at the polar/non-polar interfaces of $\text{LaAlO}_3/\text{SrTiO}_3$ [5] or the proximity effects and orbital reconstruction in superconductor/ferromagnet (SC/FM) interfaces [6–8]. All these properties are closely related to the transition metal (TM) $3d$ and oxygen $2p$ electrons and their interaction with the crystal lattice. RXR experiments have therefore in particular been performed at the TM $L_{2,3}$ edges, where the $3d$ electrons of the TM are directly probed. In this way, important information has been obtained e.g. about the spatial electron density redistribution of the Ni $3d$ electrons in $\text{LaNiO}_3/\text{LaAlO}_3$ multilayers [9] or the Co valence reconstruction at a LaCoO_3 polar film surface [10]. Moreover, employing the x-ray magnetic circular dichroism (XMCD) effect, the magnetization profile of SC/FM interfaces [11], exchanged bias systems [12, 13] and other multilayers [14–17] have been studied.

Up to now, the analysis and interpretation of reflectivity is commonly done using models such as the Parratt’s [18] or the matrix formalisms [19], where homogeneous optical properties throughout the constituent materials of a heterostructure are assumed. Although, this “slab” approach has shown to be very successful in describing off-resonant reflectivities, it is not clear if it still holds under resonance conditions. At resonance, the atomic planes containing the resonant scatterers will interact very differently with the photon beam than the non-resonant regions of the material, which immediately raises the question in how far this situation can still be described using a single n , i.e., by assuming an optically homogeneous material. Obviously, these effects are particularly important when studying any sort of electronic reconstruction at surfaces and interfaces with RXR, since they are, in fact, expected to occur on atomic length scales as well.

In this report, we investigate in detail the effects in RXR, which are caused by the rapid variations of the x-ray optical properties mentioned above. Using a single thin film of LaSrMnO_4 as a practical example, we derive analytical expressions for the reflectivity based on the Parratt's formalism in which the structure of the film is considered as layered, i.e., each plane of atoms is considered as a layer. We find that variations of n at interatomic distances can have significant effects on the RXR, even in the soft x-ray range, where the wavelength of the photons is usually considered large as compared to interatomic distances. Indeed, the sensitivity of RXR to the atomic structure of a material enables to extract information about a heterostructure like interface terminations and stacking sequences, which significantly extends the capabilities of RXR.

2. Slab versus atomic slices: theory

When calculating the reflectivity, the crystal structure of the film and how it is simplified has important consequences for the calculated intensities, especially at resonant conditions. Before we start discussing these effects in detail, we first demonstrate how significant these effects can be using the model calculations presented in Fig. 1. Here we show the theoretical reflectivities for a 8 unit cells (u.c.) thick LaSrMnO_4 (LSMO) film grown on a NdGaO_3 (NGO) substrate using three different assumptions for the film structure.

In the first model, which will be referred to as “slab” from now on, the conventional approach to reflectivity is applied, i.e., the LSMO film and the NGO substrate are described as slabs with homogeneous optical/electronic properties given by its refractive index $n(\omega)_j$ (cf. Fig.1a). In the second type of model, called “atomic slices” in the following, additional information from the crystal structure is included. As shown in Fig. 1b, the MnO_2 (MO) and LaSrO_2 (LSO) atomic layers of LSMO are represented by considering them as thin slices with corresponding refraction indices $n(\omega)_{MO}$ and $n(\omega)_{LSO}$ and thicknesses of 1.8617 Å and 4.5868 Å, respectively. The thicknesses of these slices were determined using the fractional atom positions in the unit cell [20] and the value of the experimental lattice parameter $c = 12.897$ Å of the film obtained from x-ray diffraction [21]. As we will describe below, the reflectivity is much more sensitive to different stacking sequences than to the absolute value of the chosen slice thickness. At energies close to the Mn L edges, the index of refraction $n(\omega)_j$ for all the layers in the slab as well as in the atomic slices approach were determined using experimental Mn scattering factors f' and f'' determined from x-ray absorption spectra as described in the methods section (cf. Sec. 3). Also, the average LSMO density and the total film thickness (8 u.c.) is the same for each model calculation. The NGO is again described as homogenous slab. For the atomic slices description, we further consider two different LSO and MO stacking sequences (cf. Fig. 1 c,d) and compare them with the slab model in Fig.1 a.

The calculated reflectivities using these three models are shown in Fig. 1e. As

one can see, at photon energies away from the Mn L-edge, (cf. curve at 600 eV in Fig. 1e), the reflectivities are similar to one another especially at small q_z values. In strong contrast to the off-resonant region, the calculated reflectivities at resonance differ quite dramatically depending on the model used. Furthermore, the atomic slices calculations for the different stackings are distinctly different as well (green and blue curves), showing that RXR is able to discriminate between different atomic stacking sequences. All differences between the different models become more pronounced at resonance and at larger q_z values.

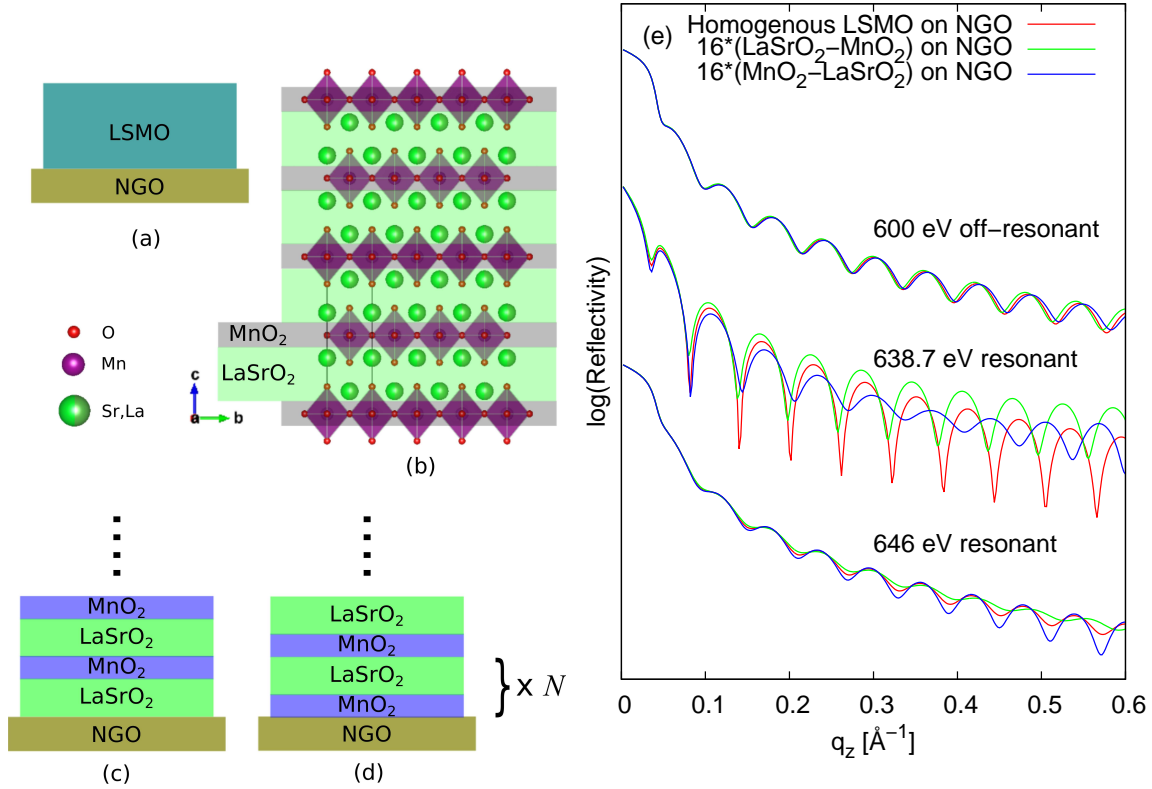


Figure 1. Comparison of calculated reflectivities for an LSMO film using three different structural models. (a) homogeneous slab, (b) the LSMO crystal structure showing the different LSO and MO atomic slices. (c) and (d) LSMO film modeled as a bilayer structure for the LSO/MO and MO/LSO stacking sequences, respectively. N refers to the number of bilayers, in this case we have $N = 16 = 8$ u.c. The average density and the total thickness is the same in each case. Note that an inversion of the layer structure, i.e. LSO/MO or MO/LSO, has a dramatic impact on the reflectivity. The refraction indices of the layers used for the calculation were determined from the experimental TEY spectra of a single layer LSMO (cf. section 3).

At first sight the strong sensitivity of RXR in the soft x-ray range to the atomic structure of the film is surprising, because the wavelength of soft x-rays is typically considered to be large compared to the inter-site spacings. For exactly this reason the internal structure is usually not taken into account when analyzing soft RXR data [9,11,15,18,22]. In order to better understand the results presented in Fig. 1 e and

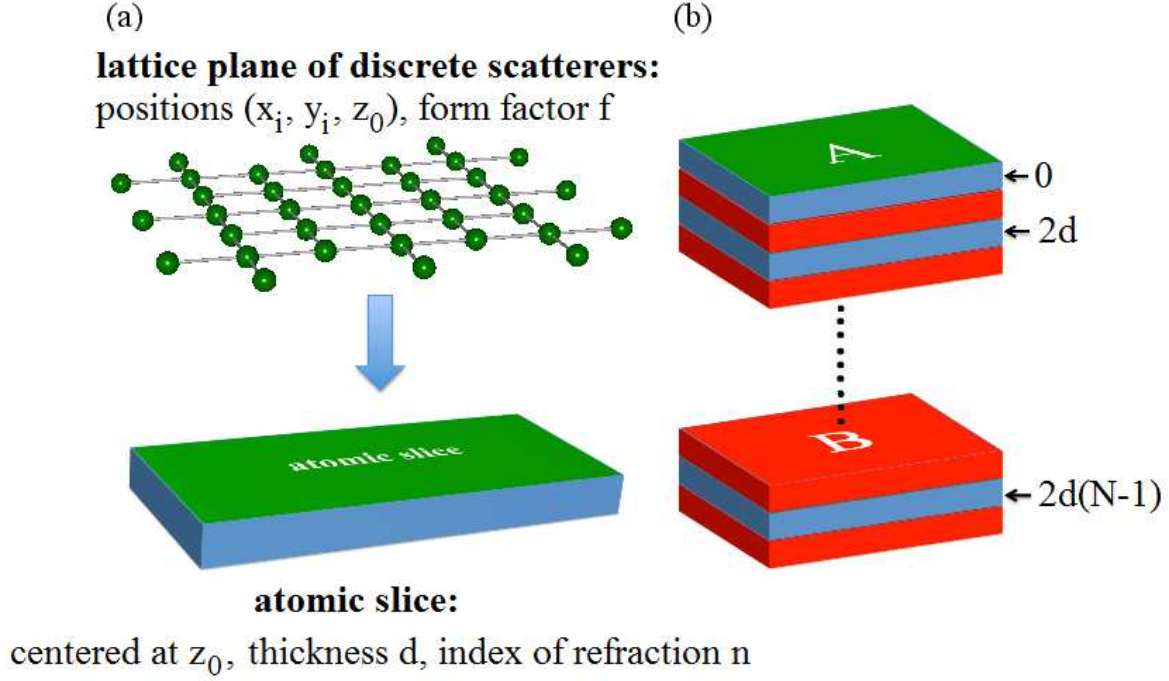


Figure 2. Atomic slice model. (a) description of atomic planes of a crystal as thin homogeneous slices with finite thickness d . (b) material whose crystal structure consists of atomic planes of different composition A and B in the atomic slice representation.

to discuss the discrepancies observed for the above mentioned models, a closer look at the atomic slice model is required. In this model we incorporate the atomic structure of the film into our analysis using thin homogeneous slices, as illustrated in Fig. 2. In this approach, the lattice planes with an area density η of discrete sites with form factor f are approximated by thin homogeneous slices with thickness $d \sim 2 \text{ \AA}$, density $\rho = \eta/d$ and index of refraction n .

To have identical scattered waves from the lattice plane and the thin slice, the index of refraction of the latter is given by the optical theorem as $n = 1 + \sum_i 2\pi\rho_i r_0 f_i / k^2$ [23], where the sum is taken over all distinct atoms in the lattice plane. Here r_0 and k are the classical electron radius and the x-ray vacuum wave vector, respectively. In this way, if only linear orders of $(1 - n)$ are taken into account, which is justified in the soft x-ray regime, the local scattering processes can be described in terms of an amplitude reflectivity r , which is in this approximation for a thin slice

$$r = \frac{2k^2}{q_z^2} (1 - n) (e^{-iq_z d/2} - e^{iq_z d/2}). \quad (1)$$

where q_z is the z component of the momentum transfer vector of the x-ray traveling through the slice. Note that the intensity reflectivity is given by $|r|^2$.

The two phase factors in the above expression correspond to the interference of rays reflected from the top and bottom interface at $\pm d/2$ of the thin slice. This interference term has been introduced artificially by the present approximation and does not exist for a single lattice plane. It is therefore important to show that this term can be neglected, i.e., to show that the dependency of r on d can be neglected. To this end, we express r , using the above expression for n ,

$$r = -\frac{4\pi\eta}{q_z}r_0f \left\{ 1 - \frac{(q_z d)^2}{24} + \mathcal{O}[(q_z d)^4] \right\}, \quad (2)$$

which shows that the interference effects caused by the two interfaces at $\pm d/2$ do not enter, as long as $(q_z d)^2/24 \ll 1$, which in turn holds as long as $d \ll \lambda/3$. This is the case for most of the soft RXR measurements where $q_z < 0.5 \text{ \AA}^{-1}$, if $d < 5 \text{ \AA}$. A very similar, more general result has been obtained in Ref [?].

Corresponding to our example LSMO, we now consider a material with two different lattice planes separated by d , which are described by two different thin slices A and B, respectively (cf. Fig. 2 (b)). The total amplitude reflectivity r_{tot} of the whole system is the sum of the scattering from all the slices with the corresponding relative phases. Using the leading order term of Eq. 2, one obtains for a film with N unit cells

$$\begin{aligned} r_{tot} &= -\frac{4\pi r_0}{q_z} \sum_{\nu=0}^{N-1} \{ \eta_A f^A + \eta_B f^B e^{iq_z d} \} e^{2iq_z \nu d} \\ &= -\frac{4\pi r_0}{q_z} \left\{ \frac{\overline{\eta f}}{1 - e^{iq_z d}} + \frac{\delta(\eta f)}{1 + e^{iq_z d}} \right\} (1 - e^{iq_z \Delta}), \end{aligned} \quad (3)$$

with $\Delta = 2Nd$ the thickness of the film, $\overline{\eta f} = (\eta_A f^A + \eta_B f^B)/2$ describing the average scattering strength of the film material and $\delta(\eta f) = (\eta_A f^A - \eta_B f^B)/2$ representing the difference of the scattering strengths of A and B. For $q_z d \ll 1$ this can be approximated by

$$r_{tot} \simeq -\frac{4i\pi r_0}{q_z^2} \left\{ \overline{\rho f} - \frac{i\delta(\rho f)}{2} \cdot q_z d \right\} (1 - e^{iq_z \Delta}), \quad (4)$$

where the term proportional to $\overline{\rho f}$ corresponds exactly to what is obtained by describing the film as a single homogeneous slab without internal structure. But from Eq. 4 it is also clear that the latter description starts to fail as soon as $\delta(\rho f)$ is not small compared to $\overline{\rho f}$ and $q_z d \sim 1$. Indeed, in soft RXR usually one lattice plane is at resonance, while the others are not, which means that $\delta(\rho f)$ will be significant precisely at resonance, while it becomes less and less important moving away from the resonance. In addition to this, $q_{z \text{ max}} \simeq 0.5 \text{ \AA}^{-1}$ at the transition metal L -edges and d in transition metal oxides is typically of the order of 2 \AA , so that at large momentum transfers $q_z d \sim 1$. The important result of our analysis is that in the soft x-ray region, the wavelength can therefore *not* always be considered infinitely large as compared to the lattice spacings.

According to the above discussion the contributions to r_{tot} , which originate from the internal atomic structure of the sample, become significant at resonance and at large

momentum transfer. These two regions are, however, most important when soft RXR is used for characterizing electronic reconstruction phenomena at interfaces.

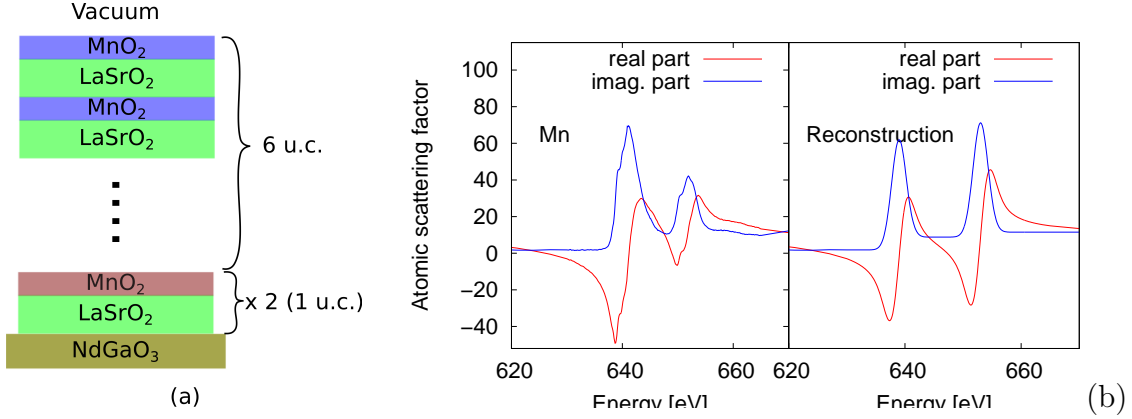


Figure 3. Electronic reconstruction of a 7 u.c. LaSrMnO_4 film. (a) Structural model used for the simulation of the reconstruction. For the first unit cell at the film/substrate interface Mn (shown in red) has an electronic reconstruction where 50% of Mn is in the $3+$ state and the rest is reconstructed. (b) Mn scattering factors, red and blue show the real and imaginary part of Mn^{3+} and of the reconstructed Mn, which was constructed to have a Gaussian shape. The real part is obtained from a Kramer-Kronig relation.

To assess the accuracy of the analysis of RXR data in terms of a standard slab model, we generated data sets consisting of reflectivities at energies close to the Mn $L_{2,3}$ edges for two layer stackings with the same total layer thicknesses of 7 u.c. (cf. figure 5 a). Additionally, the first LSMO unit cell on top of the NGO substrate was assumed to be reconstructed. Figure 3 a shows the atomic slice model with the reconstruction for a film with $\text{NGO}/N \times (\text{LSO-MO})$ stacking. For this reconstructed layer, the Mn was set to have 50% nominal Mn^{3+} scattering factors (red and blue lines in figure 3 b), as obtained from experimental XAS (cf. section 3). The other 50% Mn was assumed to be reconstructed. The scattering factors for the reconstructed Mn are shown in figure 3 b, where $f''(\omega)$ was adopted to have a Gaussian line shape with an energy shift with respect to the unreconstructed case. $f'(\omega)$ is then obtained from a Kramers-Kronig relation. As can be observed in Fig. 4 the reconstructed layer has a strong impact on the calculated reflectivities, illustrating the high sensitivity of RXR on the atomic scale.

The calculated reflectivities were then fitted with a slab model. The fitting parameters were: the measurement multiplier M , the thicknesses of the reconstructed Δ_{rec} and LSMO Δ_{LSMO} layers and the amount p_{rec} of reconstructed Mn at the interface. The results of the fits for the two different stacking orders are shown in figure 5 b and c and summarized in table 1. As seen in the table, the resulting thicknesses of the different layers are close to the starting values within an error of $\sim 1-2 \text{ \AA}$. Also, the information regarding the amount of Mn reconstruction is quite close to the original value, however, the relative errors for the fitted values of 30-40% are quite significant.

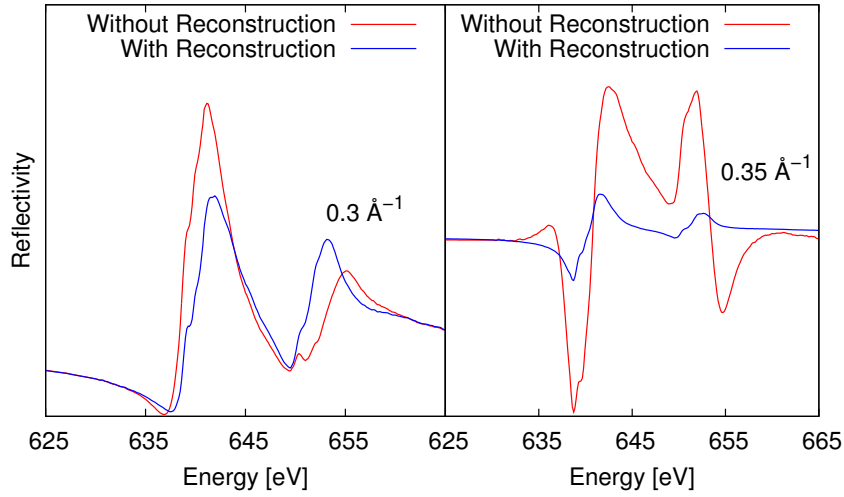


Figure 4. Reflectivity as a function of energy for two selected q_z vectors showing the effect of reconstruction.

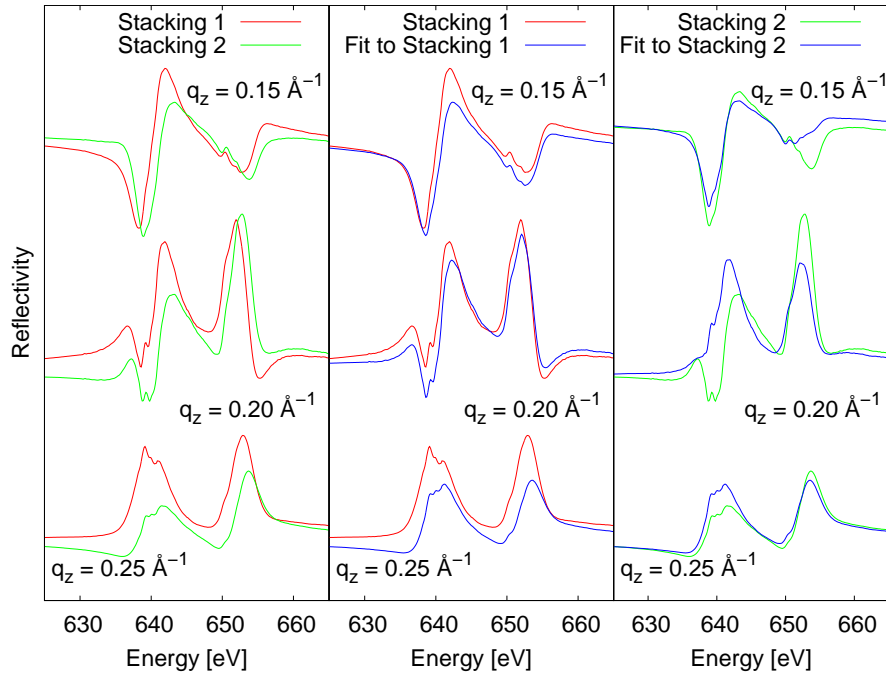


Figure 5. Calculated reflectivities from an LSMO film (7 u.c thick) grown on an NGO substrate with an artificial electronic reconstruction at the film/substrate interface. The calculated reflectivities in (a) correspond to NGO/14·[MnO₂-LaSrO₂] (stacking 1) and NGO/14·[LaSrO₂-MnO₂] (stacking 2). (b) and (c) show the fitting of the calculated reflectivities using a slab approach for stacking 1 and 2, respectively. For stacking 1, the slab approach yields a fairly good description of the reflectivity at low q_z . For stacking 2, the reflectivity lineshape can not be described very well with a slab approach. The total fitted dataset consisted of 10 reflectivities at constant energy and 10 reflectivities at constant q_z , for each polarization. For clarity only few reflectivities are shown.

Parameters	Start values	Fit to Stacking 1	Fit to Stacking 2
M	1	0.81	1.24
Δ_{LSMO} [Å]	77.38	79.76	75.18
Δ_{rec} [Å]	12.897	11.53	13.83
p_{rec} [Å]	0.5	0.45 ± 0.13	0.54 ± 0.22
χ^2	-	0.59	1.40

Table 1. Results of the fits of the calculated reflectivities for two different bilayer stacking of LSMO using the slab approach.

Based on this analysis, two main conclusions can be drawn. First, fitting RXR data using the slab approach can yield a fairly good description of the experiment. Notwithstanding, the use of the slab model introduces errors, since it simplifies the real material and its reflectivity by overlooking the contribution of the internal structure of the film. This can have important consequences: as can be seen in table 1, the fit to stacking 1 yields a reasonable χ^2 value, indicating a good fit. In contrast to this, the resulting χ^2 for the fit to stacking 2 is about 2.5 times larger than that of stacking 1, implying dubious fit results and parameters. The reflectivity curves, calculated in the atomic slices approach for stacking 2, therefore cannot be described well by a slab model, which neglects the internal structure of the material. Second, by taking into account information about the lattice structure and setting up a corresponding atomic slice model enables to retrieve important information, such as the stacking sequence, which is lost when the slab approach is implemented. Therefore, a more accurate description of the experiment is obtained when utilizing the atomic slices model.

3. Methods

A (001) oriented LaSrMnO_4 (LSMO) film was grown epitaxially on a (110) oriented NdGaO_3 substrate by the pulsed laser deposition technique. Details on the sample preparation and characterization can be found elsewhere [21].

X-ray absorption spectroscopy (XAS) and resonant x-ray reflectometry experiments have been performed at the 10ID-2 (REIXS) beamline of the Canadian Light Source (Saskatoon, Canada) [24], using linearly σ - and π -polarized light. The XAS measurements were carried out in the total electron yield (TEY) mode at two different scattering geometries and incoming beam polarizations in order to extract absorption spectra corresponding to the directions parallel and perpendicular to the film surface, i.e., $E \parallel c$ and $E \perp c$ of the LSMO, respectively. The RXR experiments were carried out at energies around the Mn $L_{2,3}$ and La $M_{4,5}$ absorption edges. The reflected intensities were collected in the fixed energy (fixE) and the fixed \mathbf{q}_z (fixQ) modes. The fixE consist of \mathbf{q}_z -scans ($\theta - 2\theta$) carried out at a fixed photon energy, whereas the fixQ refers to energy scans at a fixed scattering vector \mathbf{q}_z . The selected \mathbf{q}_z vectors correspond to maxima and minima of the thickness oscillations taken from the fixE reflectivity curve

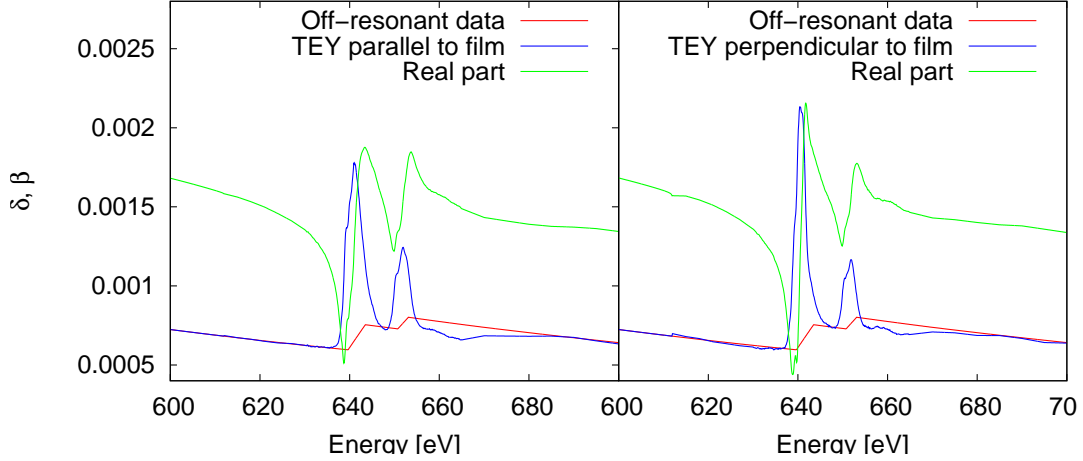


Figure 6. The optical constants δ , β of LSMO at the Mn $L_{2,3}$ edge.

measured at 641 eV. All experiments were performed at room temperature.

Determination of the imaginary part of the Mn scattering tensor and the scalar atomic scattering factors for La, Nd, Ga, Sr and O was done as described in the work by Macke *et al.* [22]. This is, the parallel and perpendicular components of the absorption spectra obtained from the XAS measurements were scaled to non-resonant tabulated values [25]. The real part is then obtained by performing a Kramers-Kronig transformation. From the atomic scattering factors we could calculate the dielectric tensor ϵ and the index of refraction $n(\omega) = 1 - \delta(\omega) + i\beta(\omega)$ of the film as shown in figure 6. The specular reflectivity was calculated with the Parratt's [18] and matrix [19] formalisms using the ReMagX suite [26].

X-ray photoelectron spectra (XPS) were recorded using PHI VersaProbe 5000 spectrometer with monochromatic Al $K\alpha$ ($h\nu = 1486.6$ eV) radiation at pass energy of 23.5 eV. In order to characterize the chemical composition of the film surface, spectra were collected as a function of the take off angle between the surface of the sample and the axis of photoelectron detector. Binding energies of the spectra were calibrated with an adventitious carbon C 1s emission line at 284.8 eV. The XPS spectra were analyzed using XPSPEAK 4.1 software after background subtraction by the Tougaard method. The shape of the characteristic peaks in all spectra was considered symmetric with a combination of 30% Lorentzian-Gaussian profile.

4. Experimental results and discussion

In order to determine a realistic model for the studied heterostructure, we characterized the film surface experimentally using XPS and determined a realistic parametrization for the LSMO/NGO interface.

4.1. Surface characterization and description of substrate/film interface

The existence of a SrO layer on the sample surface is revealed by the XPS data shown in 7a and 7b, where the take off angle dependence for Sr-3d photoemission lines is presented. As it can be seen, Sr-3d shows two sets of doublet peaks shifted by ~ 1.1 eV in binding energy indicating two different Sr-O bonds. *Peak II* shown in blue has been attributed to SrO and *peak I* (yellow) originates from Sr-O bond in the LSMO structure [27]. Since the *peak II* contribution to the spectrum measured at 20° is larger in comparison with the one measured at 45° , and considering that XPS measurements at small angles are more surface sensitive, it can be concluded that SrO segregates at the surface. Such a SrO segregation layer is commonly found on the surface of manganites [28–32]. We therefore included a SrO surface layer into the model for the reflectivity.

In addition to this segregation layer, a surface adsorption layer on top of the SrO was considered based on the fact that the sample has been exposed to air and contaminants such as water molecules, carbon etc., can be adsorbed on the sample surface. As a simplification, we consider only the scattering from oxygen in the adsorption layer.

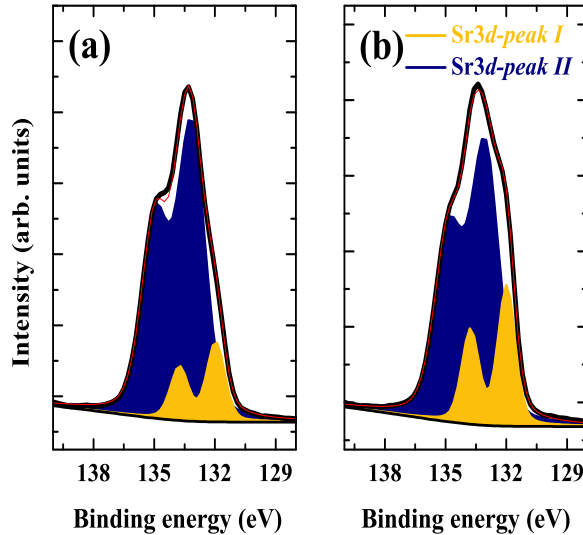


Figure 7. Angle-resolved XPS spectra of Sr-3d for LaSrMnO_4 thin film deposited on NGO (1 1 0) substrate measured at the angle of (a) 20° and (b) 45° .

Furthermore, it is known from the growth of Ruddlesden-Popper compounds on a substrate that if the c-axis of the thin film is larger than that of the substrate, the substrate terraces will lead to antiphase boundaries in the film [33,34]. Such a scenario is depicted in figure 8. From the figure it can be seen that it is relatively easy to heal antiphase boundaries in LSMO by inserting related compounds like LaMnO_3 and $\text{La}_{1.5}\text{Sr}_{1.5}\text{Mn}_2\text{O}_7$ into the stack. Once the LSMO thickness of the film increases some domains become dominating and finally the majority LSMO domain grows epitaxially. The presence of a minority phase containing single atomic layers of LaSrO_2 in this

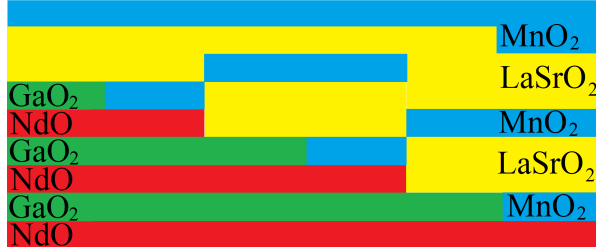


Figure 8. Antiphase boundaries of the LSMO structure when growing on an NGO substrate. Once a given thickness is reached, the film grows epitaxially.

system was also demonstrated by means of x-ray diffraction. [21] To model such an interface, a *transition* layer was included for which its index of refraction was considered to be a linear combination of that of NGO and LSMO. For this layer we have defined $n_{int} = (1 - p) \cdot n_{NGO} + p \cdot n_{LSMO}$, where the factor p was fitted during the analysis of the reflectivities.

The model used for the analysis of the experimental reflectivities hence consists of an LSMO thin film on an NGO substrate with an NGO/LSMO *transition* layer, a top SrO segregation layer, which itself is covered by a contamination layer (cf. section 4.1). Figure 9 shows representative experimental reflectivities (red) together with fits (blue) corresponding to the slab (Fig. 9a) and atomic slices approach (Fig. 9b and c). The fit results are summarized in table 2. During the fitting procedure, all the measured reflectivities at both σ and π polarization were fitted simultaneously in order to get a self-consistent result. The fitting parameters were the overall scaling factor M , thickness Δ_j of all layers and the “intermixing” parameter p of the interface layer (cf., section 4.1).

For the slab approach, the LSMO layer thickness was a fit parameter together with a Nevot & Croce roughnesses approximation at the NGO/LSMO and LSMO/SrO interfaces [35]. For the atomic slices approach, the Nevot & Croce roughness approximation is not suitable. Instead a description of the roughness at the atomic length scale is required. To achieve a description of this situation, which is depicted in fig. 8, we use a new approach that allows for a smooth transition between different materials in which the variations of the density are confined to the length scale of the corresponding atomic slice. To this end, the roughness of the LSMO layer is parametrized using a decaying error function of the form $f(z) = \text{erf}(z, \sigma) = (\sigma\sqrt{2\pi}) \int_{-\infty}^z \exp(-\zeta^2/2\sigma^2) d\zeta$. Here σ defines the width of the transition, i.e., the roughness. In order to have a smooth transition between layers modeled in the slab approach and the atomic slices of the LSMO, the layers around the interface are segmented into slices with thickness corresponding to atomic planes of the slab material.

To illustrate this, let us consider the LSMO/SrO interface as an example. The SrO is segmented into slices with density $\rho_{\text{SrO}} = 5.01 \text{ g/cm}^3$ and thickness $d_{\text{SrO}} = 2.31 \text{ \AA}$. At the LSMO/SrO-interface we then define the relative abundance S of SrO in a certain layer as

$$S = 1 - \text{erf}((z - z_0) / d_{av}, \sigma) \quad (5)$$

where z is an integer atomic slice number. z_0 is the center of the transition or, in other words, the location of the interface and d_{av} is the average atomic thickness between SrO and the LSO or MO layer at the LSMO/SrO interface. The latter parameter merely numerical and does not influence the calculated reflectivity (cf. Sec. 2). Correspondingly, the probability of finding LSMO in a given layer is defined as $L = 1 - S$.

Once L and S are determined one can then calculate new densities and thicknesses, i.e., optical constants, for the layers at the interface by summing the contributions of the SrO and LSMO layers as follows

$$\rho_{Mn}(z) = L \cdot \rho_{Mn, MnO_2-Layer} \quad \text{if } z/3 \in \mathbb{Z}, \text{ else } \rho_{Mn}(z) = 0 \quad (6)$$

$$d(z) = L \cdot d_{MnO_2} + S \cdot d_{SrO} \quad \text{if } z/3 \in \mathbb{Z} \quad (7)$$

The definitions for the other atom densities and layer thicknesses are set up in the same way. Note that this parametrization allows us to choose a given film termination at any interface of the studied heterostructure. In order to obtain stable fit results, we had to assume the same roughness σ for all interfaces. Although this obviously needs not to be fulfilled in the real heterostructure, the corresponding model fits the experimental results well (see below), indicating that the roughnesses of the different interfaces in the real material are indeed similar.

Figure 10 shows the resulting χ^2 for different terminations (z_0) of the LSMO at the LSMO/SrO interface. As shown in the figure, the lowest χ^2 is obtained when the LSMO at the interface with SrO is terminated with a MnO_2 atomic layer that contributes about $\sim 80\%$ to the interface. In comparison, the highest χ^2 , i.e., the poorest fit to the data, is obtained when the termination is $LaSrO_2$. The resulting fits for these two extreme cases are shown in fig. 9b and c, respectively and listed in table 2. This analysis allows to conclude that the best fit to the experiment is given by the case in which the LSMO film is MnO_2 terminated. Regarding the interface with the substrate, although the NGO/LSMO termination is not well defined there are two main conclusions we get from the fit results. First, the thickness of the *transition* layer is $\sim 9-10 \text{ \AA}$ (cf. table 2). This means that the region where antiphase boundaries appear is less than one LSMO unit cell in length. This, together with the obtained small roughness value ($\sim 2 \text{ \AA}$), shows that the NGO/LSMO-interface is very sharp. Second, the fits yield that the first layer that grows with few antiphase boundaries on the NGO is a single LSO layer. This is better seen in the elementary density profiles in Fig. 9e. The lines showing the interface between the *transition*/LSMO and LSMO/SrO layers corresponds to the z_0 value of the error function at that interface.

Comparing the resulting fits using both slab and atomic slices (Fig. 9 a and b, respectively) it is not obvious which yields the best description of the data. From a qualitative point of view, both models reproduce most of the features such as the thickness oscillations. Also their fit errors χ^2 are similar as shown in table 2.

Still, the fit using atomic layers has important information that is completely lost when the slab approach is used. This is the stacking sequence of the LSO and MO bilayers. Such information is of primal importance not only for crystal growers but also

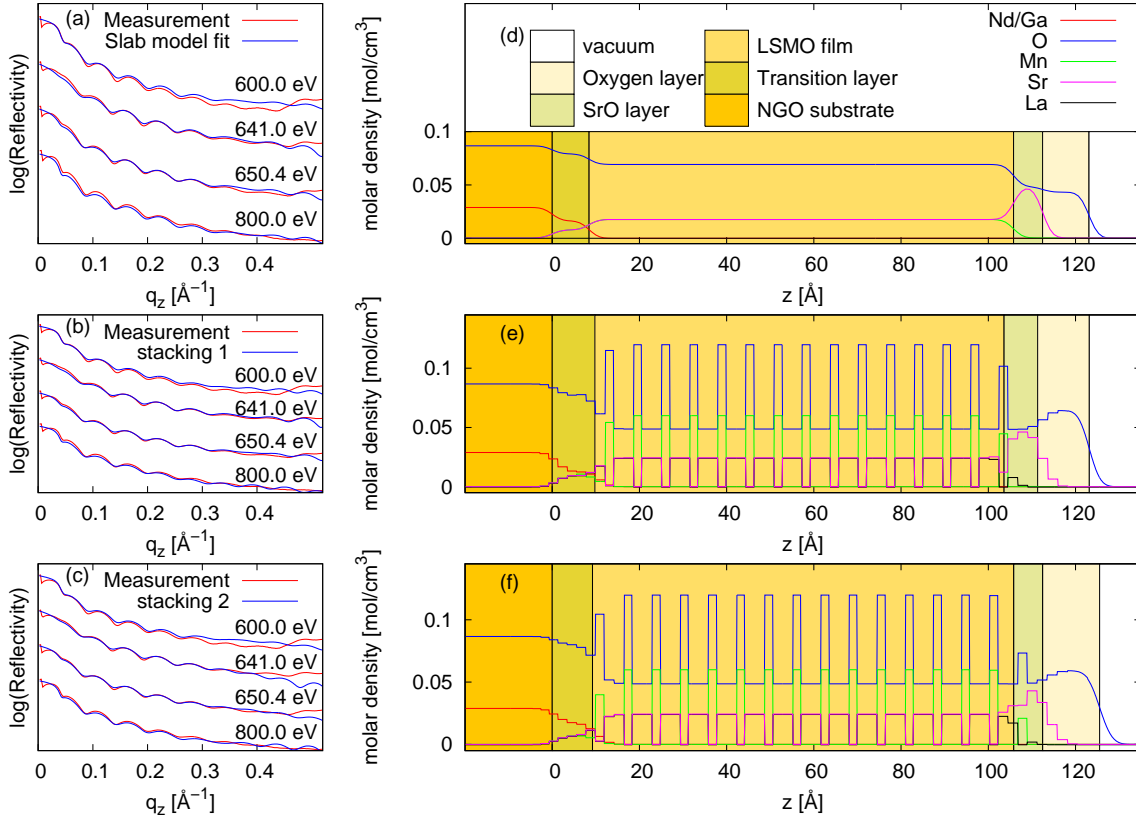


Figure 9. Selected resonant x-ray reflectivities measured close to the Mn $L_{2,3}$ edges. (a) shows the fit result based on the slab approach, (b) shows a fit result based on an atomic slices approach with the lowest χ^2 stacking, whereas (c) shows a fit result where the LSMO/SrO termination was fixed. (d), (e), and (f) show the elementary density profile throughout the film thickness for the corresponding models. The lines showing the interface between the *transition*/LSMO and LSMO/SrO layers corresponds to the z_0 value of the error function (cf. cEq. 5) at that interface.

in order to explain physical phenomena, which are determined by terminations such as the effects at the LAO/STO interfaces. This can only be retrieved by describing the film as the atomic layers that form the crystal structure.

The power of this is better seen by comparing the fits using the atomic slices approach with two different stacking sequence of the bilayers, i.e., figures 9b and c. Although, still both fits are very similar qualitatively, their χ^2 values differ considerably, thus showing that *only one* of the stacking yields proper description of the experiment. Moreover, during the fine tuning of the film structure using the atomic slices approach, we notice that for some given structural configuration, all the experimental reflectivities measured at the Mn edge were properly described. Notwithstanding, off-resonant reflectivities and those measured close to the La $M_{4,5}$ edges did not. By adding an additional LaSrO_2 atomic layer, all the reflectivities, i.e., La, Mn and off-resonant were nicely reproduced. These effects corroborate that the sensitivity given by

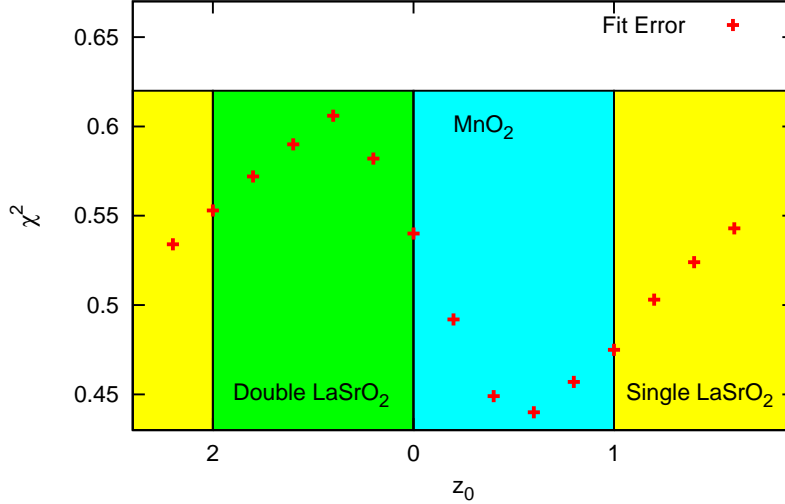


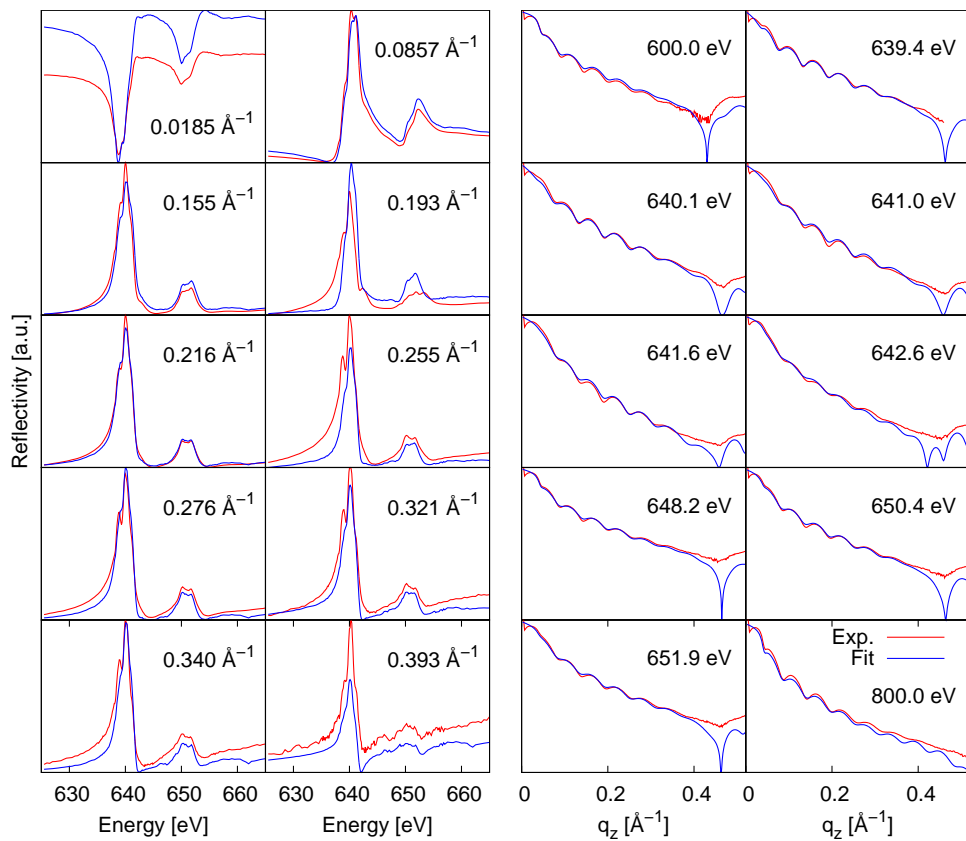
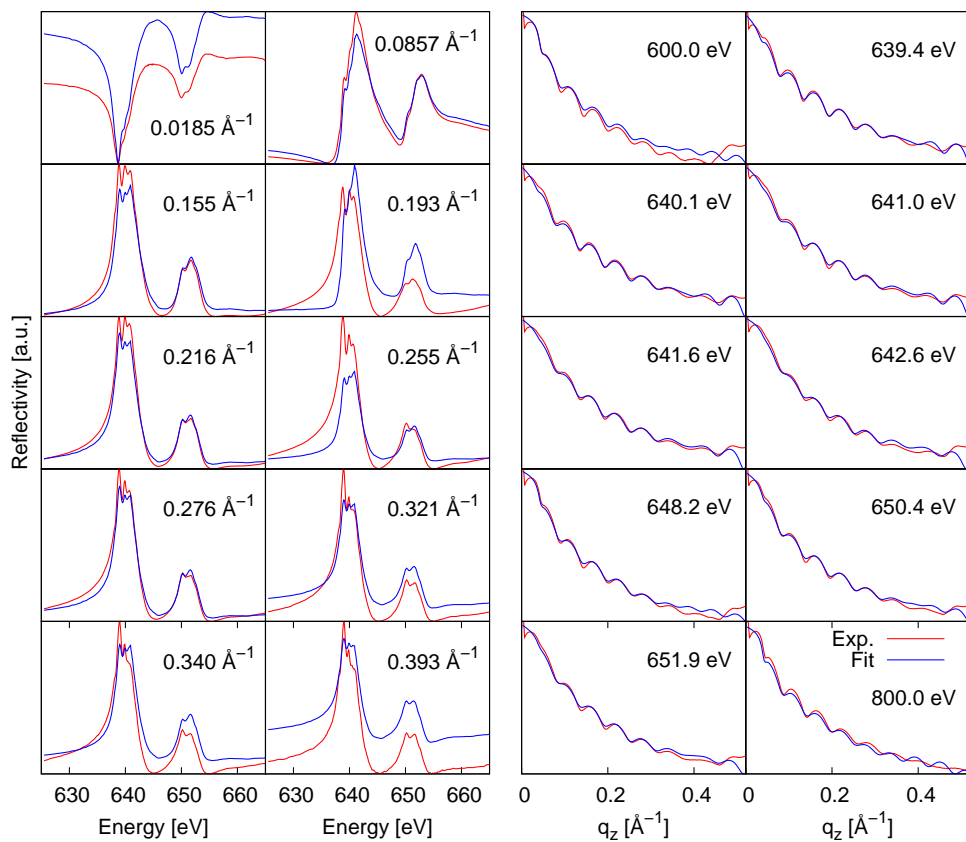
Figure 10. Fit error χ^2 for different LSMO terminations z_0 at the LSMO/SrO interface. The lowest χ^2 is obtained for a MnO_2 terminated film.

RXR experiments indeed provide atomic layer resolution with extremely high chemical sensitivity.

Figure 11 shows all the experimental reflectivities for both polarizations, together with the fit obtained with this final model. Although, there are some deviations, the overall agreement is very good. Quite remarkable is, that the polarization dependence is nicely captured. Notwithstanding this very satisfying result, the best χ^2 -value obtained here still is 0.44. Indeed, as can most clearly be observed in the fixQ-scans displayed in Fig. 11, some deviations between the model and experiment remain. More specifically, while some fixQ-profiles are nicely reproduced by the model, the modelling becomes less precise for both polarizations at certain q_z .

These deviations are most likely related to the fact that our model assumes a single Mn-species. This in particular means that we do not consider possible changes of the Mn 3d-states at the interface regions. However, as discussed above, our analysis already shows that there is a transition layer between the NGO-substrate and the LSMO-film as well as a SrO-layer at the top of the LSMO-film. The Mn-sites in these regions are therefore located in a different chemical environment than the ones inside the film. The configuration of the Mn valence shell can hence be expected to be dependent on the location of the Mn within the heterostructure. In addition to this, also symmetries are broken at interfaces and polar structures like LSMO may exhibit a so-called electronic reconstruction. Although we cannot yet determine which of these effects alters the electronic state of Mn in the interface regions to what extent, there will be variations of the Mn valence states when moving from the film bulk towards the interfaces.

As a consequence we expect that there are at least 3 different Mn-species in the NGO/LSMO heterostructure, namely (i) at the LSMO/SrO interface, (ii) in the film bulk and (iii) in the transition layer at the NGO/LSMO interface. The present model



Parameters	Slab	Atomic slices Stacking 1	Atomic slices Stacking 2
M	2.03	1.98	1.67
Δ_{trans} [Å]	8.84	9.77	9.24
Δ_{LSMO} [Å]	97.36	93.89	96.77
Δ_{SrO} [Å]	6.65	5.51	6.65
Δ_{O} [Å]	10.64	11.84	13.06
ρ_{O} [g/cm^3]	0.69	1.03	0.95
σ [Å]	1.76	2.00	2.28
p	0.56	0.56	0.41
z_0 (LSMO/SrO)	-	0.6	2.6
χ^2	0.49	0.44	0.61

Table 2. Fit results of experimental reflectivity data with different structural models. Note that a model that neglects atomic slices completely is still better than a model with wrong stacking.

only includes Mn-species (ii), corresponding to the film bulk, which we believe is the dominant reason for the remaining deviations between model and experiment.

However, determining the unknown electronic properties of the Mn-species (i) and (iii) at the interfaces by resonant reflectivity alone is challenging as it requires to enlarge the parameter set for the modelling significantly. Here still improved methods for the data analysis need to be developed that allow retrieving the electronic properties at the interfaces in a final refinement step.

5. Summary

We have shown that the atomic structure of a material can influence soft x-ray RXR profiles and hence can be very important for the analysis of RXR data. A new approach to analyzing RXR in the soft x-ray range, which takes into account the atomic structure of a material, has been developed and applied to the RXR-analysis of an LaSrMnO_4 film. The presented modelling in terms of atomic slices not only provides an improved description of the experimental data. It also enables to extract important additional information like layer termination and stacking sequence of the atomic planes of the film. This additional information is indeed of paramount importance for the understanding of relevant physical phenomena such as the 2DEG observed in LAO/STO interfaces. This renders RXR an even more powerful experimental tool to investigate artificial heterostructures and devices.

6. Acknowledgements

We thank M. Haverkort and U. Treske for fruitful discussions. M. Zwiebler, J. E. Hamann-Borrero and J. Geck gratefully acknowledge the support through the

DFG Emmy Noether Program (Grants GE-1647/2-1 and HA6470/1-1). Experiments described in this paper were performed at the Canadian Light Source, which is funded by the CFI, NSERC, NRC, CIHR, the Government of Saskatchewan, WD Canada and the University of Saskatchewan.

References

- [1] Elbio Dagotto. When oxides meet face to face. *Science*, 318(5853):1076–1077, 2007.
- [2] Pavlo Zubko, Stefano Gariglio, Marc Gabay, Philippe Ghosez, and Jean-Marc Triscone. Interface physics in complex oxide heterostructures. *Annu. Rev. Cond. Mat. Phys.*, 2(1):141–165, 2011.
- [3] J. Chakhalian, A. J. Millis, and J. Rondinelli. Whither the oxide interface. *Nat. Mater.*, 11:92, 2012.
- [4] H. Y. Hwang, Y. Iwasa, M. Kawasaki, B. Keimer, N. Nagaosa, and Y. Tokura. Emergent phenomena at oxide interfaces. *Nat. Mater.*, 11:103, 2012.
- [5] A. Ohtomo and H. Y. Hwang. A high-mobility electron gas at the $\text{LaAlO}_3/\text{SrTiO}_3$ heterointerface. *Nature*, 427:423, 2004.
- [6] A. I. Buzdin. Proximity effects in superconductor-ferromagnet heterostructures. *Rev. Mod. Phys.*, 77(3):935–976, Sep 2005.
- [7] J. Chakhalian, G. Freeland, J. W. and Srajer, J. Stremper, G. Khaliullin, J. C. Cezar, T. Charlton, R. Dalgliesh, C. Bernhard, G. Cristiani, H.-U. Habermeier, and B. Keimer. Magnetism at the interface between ferromagnetic and superconducting oxides. *Nat Phys*, 2:244, 2006.
- [8] J. Chakhalian, J. W. Freeland, H.-U. Habermeier, G. Cristiani, G. Khaliullin, M. van Veenendaal, and B. Keimer. Orbital reconstruction and covalent bonding at an oxide interface. *Science*, 318(5853):1114–1117, 2007.
- [9] Eva Benckiser, Maurits W. Haverkort, Sebastian Brück, Eberhard Goering, Sebastian Macke, Alex Frañó, Xiaoping Yang, Ole K. Andersen, Georg Cristiani, Hanns-Ulrich Habermeier, Alexander V. Boris, Ioannis Zegkinoglou, Peter Wochner, Heon-Jung Kim, Vladimir Hinkov, and Bernhard Keimer. Orbital reflectometry of oxide heterostructures. *Nat. Mater.*, 10:189–193, 2011.
- [10] J. E. Hamann-Borrero. unpublished.
- [11] S Brück, S Treiber, S Macke, P Audehm, G Christiani, S Soltan, H-U Habermeier, E Goering, and J Albrecht. The temperature-dependent magnetization profile across an epitaxial bilayer of ferromagnetic $\text{La}_{2/3}\text{Ca}_{1/3}\text{MnO}_3$ and superconducting $\text{YBa}_2\text{Cu}_3\text{O}_{7-\delta}$. *New J. Phys.*, 13(3):033023, 2011.
- [12] J. M. Tonnerre, M. De Santis, S. Grenier, H. C. N. Tolentino, V. Langlais, E. Bontempi, M. García-Fernández, and U. Staub. Depth magnetization profile of a perpendicular exchange coupled system by soft-x-ray resonant magnetic reflectivity. *Phys. Rev. Lett.*, 100:157202, Apr 2008.
- [13] Sebastian Brück, Sebastian Macke, Eberhard Goering, Xiaosong Ji, Qingfeng Zhan, and Kannan M. Krishnan. Coupling of Fe and uncompensated Mn moments in exchange-biased Fe/Mn/Pd. *Phys. Rev. B*, 81:134414, Apr 2010.
- [14] S. D. Brown, L. Bouchenoire, P. Thompson, R. Springell, A. Mirone, W. G. Stirling, A. Beesley, M. F. Thomas, R. C. C. Ward, M. R. Wells, S. Langridge, S. W. Zochowski, and G. H. Lander. Profile of the U 5f magnetization in U – Fe multilayers. *Phys. Rev. B*, 77:014427, Jan 2008.
- [15] J.M. Tonnerre, E. Jal, E. Bontempi, N. Jaouen, M. Elzo, S. Grenier, HL Meyerheim, and M. Przybylski. Depth-resolved magnetization distribution in ultra thin films by soft x-ray resonant magnetic reflectivity. *Eur. Phys. J. Special Topics*, 208:177–187, 2012.
- [16] Emmanuelle Jal, Maciej Dabrowski, Jean-Marc Tonnerre, Marek Przybylski, Stéphane Grenier, Nicolas Jaouen, and Jürgen Kirschner. Magnetization profile across Au-covered bcc Fe films grown on a vicinal surface of Ag(001) as seen by x-ray resonant magnetic reflectivity. *Phys. Rev. B*, 87:224418, Jun 2013.

- [17] Nobuyoshi Hosoi, Takuo Ohkuchi, Kenji Kodama, and Motohiro Suzuki. Charge and induced magnetic structures of au layers in fe/au bilayer and fe/au/fe trilayer films by resonant x-ray magnetic reflectivity at the au l_3 absorption edge. *J. Phys. Soc. Jpn.*, 83(2):024704, 2014.
- [18] L. G. Parratt. Surface studies of solids by total reflection of x-rays. *Phys. Rev.*, 95:359–369, Jul 1954.
- [19] Dwight W. Berreman. Optics in stratified and anisotropic media: 4×4 -matrix formulation. *J. Opt. Soc. Am.*, 62(4):502–510, Apr 1972.
- [20] M.A. Ghebouli, B. Ghebouli, A. Bouhemadou, M. Fatmi, and K. Bouamama. Structural, electronic, optical and thermodynamic properties of $\text{sr}_x\text{ca}_{1-x}\text{o}$, $\text{ba}_x\text{sr}_{1-x}\text{o}$ and $\text{ba}_x\text{ca}_{1-x}\text{o}$ alloys. *Journal of Alloys and Compounds*, 509(5):1440 – 1447, 2011.
- [21] Mehran Vafae, Mehrdad Baghaie Yazdi, Aldin Radetinac, Gennady Cherkashinin, Philipp Komissinskiy, and Lambert Alf. Strain engineering in epitaxial $\text{la}_{1-x}\text{sr}_{1+x}\text{mno}_4$ thin films. *J. Appl. Phys.*, 113(5):053906, 2013.
- [22] Sebastian Macke, Abdullah Radi, Jorge E. Hamann-Borrero, Martin Bluschke, Sebastian Brück, Eberhard Goering, Ronny Sutarto, Feizhou He, Georg Cristiani, Meng Wu, Eva Benckiser, Hanns-Ulrich Habermeier, Gennady Logvenov, Nicolas Gauquelin, Gianluigi A. Botton, Adam P. Kajdos, Susanne Stemmer, Georg A. Sawatzky, Maurits W. Haverkort, Bernhard Keimer, and Vladimir Hinkov. Element specific monolayer depth profiling. *Adv. Mater.*, pages n/a–n/a, 2014.
- [23] Jens Als-Nielsen and Des McMorrow. *Elements of modern x-ray physics*. Wiley, Chichester, England, 2011.
- [24] D. G. Hawthorn, F. He, L. Venema, H. Davis, A. J. Achkar, J. Zhang, R. Sutarto, H. Wadati, A. Radi, T. Wilson, G. Wright, K. M. Shen, J. Geck, H. Zhang, V. Novák, and G. A. Sawatzky. An in-vacuum diffractometer for resonant elastic soft x-ray scattering. *Rev. Sci. Instrum.*, 82(7):073104, 2011.
- [25] C. T. Chantler. Theoretical form factor, attenuation, and scattering tabulation for $z=1-92$ from $e=1-10$ ev to $e=0.4-1.0$ mev. *J. Phys. Chem. Ref. Data*, 24(1):71–643, 1995.
- [26] Sebastian Macke, Abdullah Radi, Jorge E. Hamann-Borrero, Adriano Verna, Martin Bluschke, Sebastian Brück, Eberhard Goering, Ronny Sutarto, Feizhou He, Georg Cristiani, Meng Wu, Eva Benckiser, Hanns-Ulrich Habermeier, Gennady Logvenov, Nicolas Gauquelin, Gianluigi A. Botton, Adam P. Kajdos, Susanne Stemmer, Georg A. Sawatzky, Maurits W. Haverkort, Bernhard Keimer, and Vladimir Hinkov. Element specific monolayer depth profiling. *Advanced Materials*, pages n/a–n/a, 2014.
- [27] R Bertacco, J.P Contour, A Barthélemy, and J Olivier. Evidence for strontium segregation in $\text{la}_{0.7}\text{sr}_{0.3}\text{mno}_3$ thin films grown by pulsed laser deposition: consequences for tunnelling junctions. *Surface Science*, 511(1-3):366 – 372, 2002.
- [28] Tim T. Fister, Dillon D. Fong, Jeffrey A. Eastman, Peter M. Baldo, Matthew J. Highland, Paul H. Fuoss, Kavaipatti R. Balasubramaniam, Joanna C. Meador, and Paul A. Salvador. In situ characterization of strontium surface segregation in epitaxial $\text{la}_{0.7}\text{sr}_{0.3}\text{mno}_3$ thin films as a function of oxygen partial pressure. *Appl. Phys. Lett.*, 93(15):151904, 2008.
- [29] Khabiboulakh Katsiev, Bilge Yildiz, Kavaipatti Balasubramaniam, and Paul A. Salvador. Electron tunneling characteristics on $\text{la}_{0.7}\text{sr}_{0.3}\text{mno}_3$ thin-film surfaces at high temperature. *Appl. Phys. Lett.*, 95(9):–, 2009.
- [30] P. Abellán, C. Moreno, F. Sandiumenge, X. Obradors, and M.-J. Casanove. Misfit relaxation of $\text{la}_{0.7}\text{sr}_{0.3}\text{mno}_3$ thin films by a nanodot segregation mechanism. *Appl. Phys. Lett.*, 98(4):–, 2011.
- [31] Zhipeng Li, Michel Bosman, Zhen Yang, Peng Ren, Lan Wang, Liang Cao, Xiaojiang Yu, Chang Ke, Mark B. H. Breese, Andriwo Rusydi, Weiguang Zhu, Zhili Dong, and Yong Lim Foo. Interface and surface cation stoichiometry modified by oxygen vacancies in epitaxial manganite films. *Adv. Funct. Mater.*, 22(20):4312–4321, 2012.
- [32] L. Poggini, S. Ninova, P. Graziosi, M. Mannini, V. Lanzilotto, B. Cortigiani, L. Malavolti, F. Borgatti, U. Bardi, F. Totti, I. Bergenti, V. A. Dediu, and R. Sessoli. A combined ion

- scattering, photoemission, and dft investigation on the termination layer of a $\text{La}_{0.7}\text{Sr}_{0.3}\text{MnO}_3$ spin injecting electrode. *The Journal of Physical Chemistry C*, 118(25):13631–13637, 2014.
- [33] T. Haage, J. Zegenhagen, J. Q. Li, H.-U. Habermeier, M. Cardona, Ch. Jooss, R. Warthmann, A. Forkl, and H. Kronmüller. Transport properties and flux pinning by self-organization in $\text{YBa}_2\text{Cu}_3\text{O}_{7-\delta}$ films on vicinal $\text{SrTiO}_3(001)$. *Phys. Rev. B*, 56:8404–8418, Oct 1997.
- [34] V. K. Malik, I. Marozau, S. Das, B. Doggett, D. K. Satapathy, M. A. Uribe-Laverde, N. Biskup, M. Varela, C. W. Schneider, C. Marcelot, J. Stahn, and C. Bernhard. Pulsed laser deposition growth of heteroepitaxial $\text{YBa}_2\text{Cu}_3\text{O}_7/\text{La}_{0.67}\text{Ca}_{0.33}\text{MnO}_3$ superlattices on NdGaO_3 and $\text{Sr}_{0.7}\text{La}_{0.3}\text{Al}_{0.65}\text{Ta}_{0.35}\text{O}_3$ substrates. *Phys. Rev. B*, 85:054514, Feb 2012.
- [35] L. Nevot and P. Croce. Caractérisation des surfaces par réflexion rasante de rayons x. application à l'étude du polissage de quelques verres silicates. *Revue de Physique appliquée*, 15(3):761–779, 1980.